THE ASTROPHYSICAL JOURNAL, 431:604–616, 1994 August 20

A MODEL FOR COLLISIONALLY INDUCED DISTURBED STRUCTURE IN DISK GALAXIES

RICHARD A. GERBER[1] AND SUSAN A. LAMB[2]
Departments of Physics and Astronomy, University of Illinois at Urbana-Champaign
Received 1993 April 16; accepted 1994 February 18

ABSTRACT

We derive analytic expressions, using the impulse and epicycle approximations, which describe the kinematic response of a disk galaxy following a collision with a second spherical galaxy which collides perpendicular to, but not through the center of, the disk. This model can reproduce the morphologies found in *n*-body experiments in which distant encounters produce two-armed spiral patterns and more central collisions produce rings in the disk galaxy, thereby confirming that simple kinematics can be used to describe the early evolution of these systems. Application of this procedure provides a convenient method with which to conduct parameter studies of these collisions.

Comparison of the kinematic description with a fully self-gravitating, three-dimensional *n*-body/gasdynamics computer model shows that the disk galaxy's response is initially well represented by the kinematic model but that the self-gravity of the disk becomes important at longer times after the collision. The flows of gas and stars decouple from one another where stellar orbits cross, leaving regions of elevated gas density behind as the stars move freely past each other. If star formation rates are enhanced in these regions of high gas density, active star formation could be taking place where there is no corresponding dense feature in the old stellar population.

Subject headings: galaxies: interactions — galaxies: kinematics and dynamics

1. INTRODUCTION

Lynds & Toomre (1976) and Toomre (1978) showed that transient global rings could be induced in a disk galaxy if it is hit perpendicularly to the disk by a smaller spherical galaxy. Observations of ring galaxies which likely formed in this manner show that many appear to have had recent episodes of vigorous star formation in the ring, as evidenced by high levels of far-infrared emission (Appleton & Struck-Marcell 1987a), blue spectral colors (e.g., Schultz et al. 1990; Thompson & Theys 1978), strong Hα spectral lines (Fosbury & Hawarden 1977), and near-infrared and optical colors (Marcum, Appleton, & Higdon 1992). Example systems include VII Zw 466 (Thompson & Theys 1978), Arp 147 (Schultz et al. 1990, 1991), and the Cartwheel galaxy (Marcum et al. 1992; Struck-Marcell & Higdon 1993; Higdon 1993). The basic picture that a nearly axisymmetric collision produces an outward propagating ring of high density and high star formation rate has been worked out by a number of investigators (Theys & Spiegel 1976, 1977; Chatterjee 1984; Appleton & Struck-Marcell 1987b; Struck-Marcell & Appleton 1987; Huang & Stewart 1988; Struck-Marcell & Lotan 1990; Gerber, Lamb, & Balsara 1992; Hernquist & Weil 1993; Gerber 1993).

If the collision is not axisymmetric, off-center rings, arcs, and spiral patterns can be formed (Toomre & Toomre 1972; Toomre 1978; Struck-Marcell 1990; Chatterjee 1986; Huang & Stewart 1988; Gerber, et al. 1992). In order to understand the mechanism by which off-center collisions produce disturbed morphologies in galactic disks, a simplified analytic model can provide insight. Further, an analytic model can be simply and economically used to explore parameter space and guide the choice of computationally expensive three-dimensional gravitational and hydrodynamical computation models of observed systems. In this paper we show that the disk morphologies produced by Toomre's (1978) *n*-body experiments on ring galaxies (see also Byrd & Howard 1992) can be understood in terms of an impulsive encounter with a second galaxy which produces epicyclic oscillations in the disk galaxy (see § 2; Binney & Tremaine 1987; Struck-Marcell & Lotan 1990). Some of the results obtained here are similar to those obtained by Struck-Marcell (1990) in a study of caustic development in slightly off center collisions. Donner, Engström, & Sundelius (1991) have pursued a similar study in the context of the generation of spiral arm patterns. The motivation for the present study is to gain insight into the mechanism whereby high gas density regions are produced in numerical *n*-body/gasdynamics simulations of ring galaxies (Gerber et al. 1992; Gerber 1993; Gerber, Lamb, & Balsara 1994a; Struck-Marcell & Higdon 1993; Hernquist & Weil 1993). Unlike Struck-Marcell (1990), we explicitly include an arbitrarily large impact parameter and do not restrict the magnitude of the azimuthal velocity impulse in comparison to the radial velocity impulse.

We derive analytic expressions to describe the kinematic evolution of a stellar disk perturbed by the collision of a second galaxy, which moves on a trajectory perpendicular to the disk but does not pass through its center. The intruding galaxy is taken to be spherical, and the disk stars move in a rigid potential that produces a constant circular rotation velocity. We show that the resulting morphologies depend on three quantities; a "strength" parameter (see § 2), the impact parameter, and the central concentration of the spherical galaxy.

The purely kinematic model cannot yield information about the role of self-gravity and gasdynamical processes, which are likely important for determining the sites of elevated star formation rates. To learn more about these processes we compare the behavior predicted by our analytic expressions with computational results from a fully self-gravitating three-

[1] Postal address: NASA/Ames Research Center, Space Sciences Division, Theoretical Studies Branch, Mail Stop 245-3, Moffett Field, CA 94035.
[2] Postal address: Department of Astronomy, University of Illinois at Urbana-Champaign, Urbana, IL 61801.

dimensional n-body/gasdynamics code (Balsara 1990; Gerber et al. 1994a). The code employs a combination of n-body particle-mesh (PM) and smoothed particle hydrodynamics (SPH) techniques. The initial behavior of the galaxies is similar to that predicted by our analytic model, but at later times in the evolution of the disk, self-gravity becomes important in amplifying density enhancements (see also Donner et al. 1991). Gas piles up where orbits cross since, unlike the stars, gas cannot freely move through regions where orbits intersect. These regions of high gas density are likely to be the locations of active star formation.

Our analytic model for the velocity impulse is described in § 2. The kinematic response predicted by the model is presented in § 3. In § 4, a detailed study of one collision is used to demonstrate the technique developed and to explore the comparison between the analytic and numerical results. A summary is given in § 5.

2. ANALYTIC MODEL

Under the simplifying assumptions described in the following sections, we derive the two-dimensional equations of motion for disk stars following a collision with a spherically symmetric galaxy. This intruder hits the disk at normal incidence at an arbitrary distance from the center. Using these equations of motion, which are shown to be functions of a star's initial position and three dimensionless parameters which are defined below, we can determine the kinematic morphology of the disk at any arbitrary time after the collision.

2.1. *Solution for Velocity Impulses*

We first solve for the velocity impulse delivered by the intruder as it passes through the disk galaxy at constant velocity. The impulse approximation is expected to be valid as long as the intruder moves fast enough that the disk stars do not have time to move appreciably in their orbits during the interaction, but as mentioned in Binney & Tremaine (1987), this method can often be applied beyond its formal limits.

The geometry we assume is illustrated in Figure 1. The disk lies in the x-y plane. The intruder proceeds in a straight line in the x-z plane (the plane of the paper) parallel to the z axis at constant velocity V and penetrates the disk at a distance $x = b$ from the center of the disk. The vector $\boldsymbol{r}$ denotes position with respect to the center of the intruder, while the vector $\boldsymbol{R}$, as well as the coordinates (x, y, z), refer to position with respect to the center of the disk.

We represent the intruder with a Plummer model (Plummer 1911); it provides an analytic model of a softened potential, and the degree of central concentration can be easily varied. The gravitational potential of the Plummer model is given by

$$\Phi = -\frac{GM}{(r^2 + a^2)^{1/2}}, \tag{1}$$

where G is the gravitational constant, M is the total mass of the Plummer model, and a is a constant, often referred to as a "softening" length since it introduces a length scale into the potential and prevents singular behavior at the origin. The velocity impulse delivered to a particle at a position r from the intruder is

$$\Delta \boldsymbol{v}(\boldsymbol{r}) = -\int_{-\infty}^{\infty} \nabla\Phi(\boldsymbol{r}, t)dt\,. \tag{2}$$

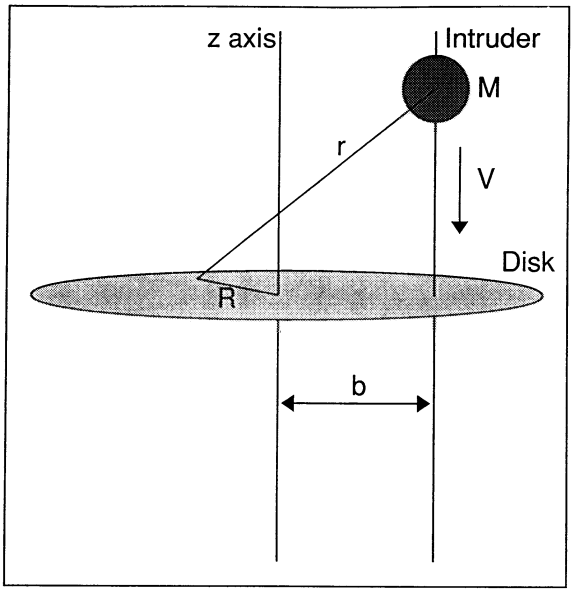

FIG. 1.—The geometrical configuration for the derivation of the impulse approximation expressions. The z-axis passes through the disk's center, and the intruder moves along a line parallel to the z-axis, intersecting the plane of the disk a distance b from its center. The intruder, of mass M, moves at constant velocity V.

Substituting $\boldsymbol{r}(t) = (x - b)\hat{\boldsymbol{x}} + y\hat{\boldsymbol{y}} + (z + Vt)\hat{\boldsymbol{z}}$, and taking the gradient of the potential yields,

$$(\nabla\Phi)_x = -\frac{GM(x - b)}{[(x - b)^2 + (z + Vt)^2 + y^2 + a^2]^{3/2}}, \tag{3a}$$

$$(\nabla\Phi)_y = -\frac{GM_y}{[(x - b)^2 + (z + Vt)^2 + y^2 + a^2]^{3/2}}, \tag{3b}$$

$$(\nabla\Phi)_z = -\frac{GM(z + Vt)}{[(x - b)^2 + (z + Vt)^2 + y^2 + a^2]^{3/2}}. \tag{3c}$$

Upon performing the integrations of equation (2), we obtain

$$\Delta \boldsymbol{v}(x, y, z) = -\frac{2GM}{V}\left[\frac{(x - b)\hat{\boldsymbol{x}} + y\hat{\boldsymbol{y}}}{(x - b)^2 + y^2 + a^2}\right]. \tag{4}$$

Rewriting this result in polar coordinates, (R, ϕ) defined by $x = R\cos\phi$, $y = R\sin\phi$, gives

$$\Delta \boldsymbol{v}(R, \phi) = -\frac{2GM}{V}\left[\frac{(R - b\cos\phi)\hat{\boldsymbol{R}} + b\sin\phi\hat{\boldsymbol{\phi}}}{R^2 - 2Rb\cos\phi + b^2 + a^2}\right]. \tag{5}$$

We write the angular dependence in dimensionless form by defining the dimensionless parameters, $\eta \equiv R/b$ and $\gamma \equiv a/b$ and have

$$\Delta v_R = -\frac{2GM}{bV}\left(\frac{\eta - \cos\phi}{\eta^2 - 2\eta\cos\phi + 1 + \gamma^2}\right), \tag{6a}$$

$$\Delta v_\phi = -\frac{2GM}{bV}\left(\frac{\sin\phi}{\eta^2 - 2\eta\cos\phi + 1 + \gamma^2}\right). \tag{6b}$$

2.2. *Response to the Impulse*

We here investigate how the velocity impulse affects the orbits of stars in a given nonchanging potential. Our analysis is somewhat similar to those given in Struck-Marcell (1990) and

Donner et al. (1991), with the differences that 1) motion of the host galaxy nucleus is considered; 2) a flat rotation curve in the target galaxy is used, which yields simpler expressions; and 3) the equations of motion are given here in terms of the velocity perturbation and dimensionless collision parameters. First, we modify equations (6) to express the velocity impulse relative to the impulse delivered to the center of the potential. In this we assume that the mass distribution that produces the halo potential, although not explicitly modeled here, reacts to the intruder's passage by acquiring the velocity that would have been delivered to a particle at the center of the disk. The equations of motion are then given in an inertial coordinate system in which the center of the potential is at rest. If we neglect this term, tidal stretching in the disk is reduced, and the morphologies produced by our approximate analytical model are less consistent with the full n-body results given in § 4.

Subtracting the velocity impulse delivered to the origin of coordinates from equations (6), we get

$$\Delta v_R = -\frac{2GM}{bV}\left(\frac{\eta - \cos\phi}{\eta^2 - 2\eta\cos\phi + 1 + \gamma^2} + \frac{\cos\phi}{1+\gamma^2}\right), \quad (7a)$$

$$\Delta v_\phi = -\frac{2GM}{bV}\left(\frac{\sin\phi}{\eta^2 - 2\eta\cos\phi + 1 + \gamma^2} - \frac{\sin\phi}{1+\gamma^2}\right). \quad (7b)$$

We obtain the equations of motion for the disk particles by assuming they were in circular orbits prior to receiving the impulse. After the interaction, a particle orbit is described as executing epicyclic motion about a guiding center on a circular orbit of radius R_g. The value of R_g is obtained by determining the radius of the circular orbit that has the same angular momentum as the particle after it received the impulse. The specific angular momentum, l_z, of a particle after the impulse is the sum of its initial angular momentum and the change in angular momentum delivered by the intruder,

$$l_z = R_0 v_{c,0} + R_0 \Delta v_\phi , \quad (8)$$

where R_0 is the initial radius and $v_{c,0}$ is the initial circular speed. The angular momentum associated with the guiding center's circular orbit is $R_g v_{c,g}$, where $v_{c,g}$ is the orbital speed of the guiding center. Equating the two expressions for the angular momentum and solving for R_g yields

$$R_g = R_0\left(\frac{v_{c,0}}{v_{c,g}} + \frac{\Delta v_\phi}{v_{c,g}}\right). \quad (9)$$

At this point the analysis is significantly simplifed if we assume that the disk galaxy particles move in a potential which produces a rotation curve which is constant with radius. This is a reasonable simplification since most disk galaxies are observed to have constant rotation curves over all but the inner portions of their disks. Under this assumption, the previous equation becomes

$$R_g = R_0\left(1 + \frac{\Delta v_\phi}{v_c}\right), \quad (10)$$

where v_c is the constant circular speed in the disk. The radial position of a particle in the epicycle approximation is

$$R = R_g + A_R \sin(\kappa t + \Psi), \quad (11)$$

where κ is the epicycle frequency (determined by the potential) and A_R and Ψ are constants to be determined from initial conditions. For a particle which was initially at coordinates (R_0, ϕ_0) we demand that $R(t=0) = R_0$ and $\dot{R}(t=0) = \Delta v_R$, note that $\kappa = \sqrt{2}v_c/R$ for the flat rotation curve potential under consideration, and find, to lowest order in velocities,

$$\tan\Psi = -\sqrt{2}\frac{\Delta v_\phi}{\Delta v_R}. \quad (12)$$

Equivalently, we can write

$$\sin\Psi = -\sqrt{2}\frac{\Delta v_\phi}{\sqrt{2\Delta v_\phi^2 + \Delta v_R^2}}, \quad (13)$$

and

$$\cos\Psi = \frac{\Delta v_R}{\sqrt{2\Delta v_\phi^2 + \Delta v_R^2}}. \quad (14)$$

The amplitude to first order is

$$A_R = R_0\frac{|\Delta\tilde{v}|}{\sqrt{2}v_c}, \quad (15)$$

where $|\Delta\tilde{v}| \equiv \sqrt{2\Delta v_\phi^2 + \Delta v_R^2}$. The expression for the radius then becomes

$$R = R_0\left[1 + \frac{\Delta v_\phi}{v_c} + \frac{|\Delta\tilde{v}|}{\sqrt{2}v_c}\sin(\kappa t + \Psi)\right]. \quad (16)$$

Note that the factors of $\sqrt{2}$ in the preceding equations are unique to the potential under consideration.

We find the expression for the angular coordinate by demanding that angular momentum be conserved along the orbit after the impulse. Equating the angular momentum after the collision with the angular momentum of the new guiding center, we have

$$\dot{\phi}R^2 = v_c R_g . \quad (17)$$

Substituting the expression for R and keeping terms only to first order, we obtain

$$\dot{\phi} = \frac{v_c}{R_g}\left[1 - \frac{2A_R}{R_0}\sin(\kappa t + \Psi)\right]. \quad (18)$$

This is integrated to give

$$\phi = \frac{v_c t}{R_0} + \frac{2A_R v_c}{\kappa R_0^2}\cos(\kappa t + \Psi) + \text{constant} . \quad (19)$$

The constant is obtained by setting $\phi(0) = \phi_0$ (as per the impulse approximation), which yields

$$\phi = \phi_0 - \frac{\Delta v_R}{v_c} + \frac{v_c t}{R_0}\left(1 - \frac{\Delta v_\phi}{v_c}\right) + \frac{|\Delta\tilde{v}|}{v_c}\cos(\kappa t + \Psi) . \quad (20)$$

We now define the following dimensionless parameters, which will prove useful later,

$$\chi \equiv \frac{2GM}{bVv_c}, \quad (21a)$$

$$\eta_{\max} \equiv \frac{R_{\max}}{b}, \quad (21b)$$

$$\gamma' \equiv \frac{\gamma}{\eta_{\max}} = \frac{a}{R_{\max}}, \quad (21c)$$

$$\tau \equiv \frac{v_c t}{2\pi R_{\max}}, \quad (21d)$$

where R_{max} is the maximum radial extent of the disk. Defined in this manner, χ is a parameter describing the "strength" of the interaction—$\chi/2\gamma$ is the maximum possible value of the velocity impulse in units of the (constant) circular speed in the disk. For our approximations to be formally valid, $\chi/2\gamma$ must be less than one. The term η_{max} is the maximum extent of the disk in units of the impact parameter, and γ' is the ratio of the intruder softening length to the maximum disk radius. The term τ measures time in units of the rotation period of the outer edge of the disk.

We define dimensionless velocity impulses to be

$$\Delta u_R \equiv \frac{\Delta v_R}{v_c \chi} = -\left(\frac{\eta_0 - \cos\phi_0}{\eta_0^2 - 2\eta_0\cos\phi_0 + 1 + \gamma'^2\eta_{max}^2} + \frac{\cos\phi_0}{1 + \gamma'^2\eta_{max}^2}\right), \tag{22a}$$

$$\Delta u_\phi \equiv \frac{\Delta v_\phi}{v_c \chi} = -\left(\frac{\sin\phi_0}{\eta_0^2 - 2\eta_0\cos\phi_0 + 1 + \gamma'^2\eta_{max}^2} - \frac{\sin\phi_0}{1 + \gamma'^2\eta_{max}^2}\right), \tag{22b}$$

$$|\Delta\tilde{u}| \equiv \frac{|\Delta\tilde{v}|}{v_c\chi} = \sqrt{2\Delta u_\phi^2 + \Delta u_R^2}\,, \tag{22c}$$

and we write the equations of motion, in terms of the ratio of radius to impact parameter η, as

$$\eta = \eta_0\left\{1 + \chi\Delta u_\phi + \frac{\chi|\Delta\tilde{u}|}{\sqrt{2}}\sin\left[2\pi\sqrt{2}\,\frac{\eta_{max}}{\eta_0}(1 - \chi\Delta u_\phi)\tau + \Psi\right]\right\} \tag{23a}$$

$$\phi = \phi_0 - \chi\Delta u_R + 2\pi\,\frac{\eta_{max}}{\eta_0}(1 - \chi\Delta u_\phi)\tau + \chi|\Delta\tilde{u}|\cos\left[2\pi\sqrt{2}\,\frac{\eta_{max}}{\eta_0}(1 - \chi\Delta u_\phi)\tau + \Psi\right]. \tag{23b}$$

We note that these equations of motion depend only on the initial coordinates, (η_0, ϕ_0), and the three parameters χ, η_{max}, and γ'.

2.3. *Surface Density*

With the particle positions as functions of time and their original coordinates, we can demand that the mass, dM, in a small area be conserved, and we get an expression for the surface density, Σ:

$$dM = \Sigma(R, \phi, t)R\,dR\,d\phi = \Sigma(R_0, \phi_0)R_0\,dR_0\,d\phi_0\,. \tag{24}$$

The coordinates are related through the determinant of the Jacobian matrix, J, by

$$dR\,d\phi = |J|\,dR_0\,d\phi_0\,. \tag{25}$$

The surface density is

$$\Sigma(R, \phi) = \Sigma(R_0, \phi_0)\,\frac{R_0}{R}\,|J|^{-1}\,. \tag{26}$$

Formally, the surface density goes to infinity at the zeros of the Jacobian (see Donner et al. 1991). The points correspond to the caustics described by Struck-Marcell (1990), Struck-Marcell & Lotan (1990), and Donner et al. (1991)—regions where orbits overlap. Many of the morphologies presented in the next section can be discussed in terms of these caustics and have been done so by Struck-Marcell (1990). In real galaxies these infinities are suppressed since 1) the density distribution is made up of discrete stars, more than one of which cannot occupy the same location, and 2) the stars are initially spread in phase space by virtue of a nonzero velocity dispersion, which will tend to suppress caustic formation. Hydrodynamic pressure forces (operating in three dimensions) help prevent infinite densities in the gaseous component of galaxies. Nevertheless, high densities are reached when gas interacts in these regions, as we will show in § 4.

3. KINEMATIC RESPONSE OF THE DISK

After the collision, the transient disk morphology at any given time is a function of the three parameters which represent 1) the impact parameter, 2) the "strength," and 3) the central concentration of the intruder. The best way to get a feel for how the three parameters affect the collision is to plot a sample of disk "stars" for different values of the parameters.

3.1. *A Survey of Forms*

The form of the equations of motion in equations (23) allows us to investigate grazing collisions by setting $\eta_{max} \leq 1$. More central collisions can be modeled by considering larger values of η_{max}. The other two parameters which govern the kinematic response of the disk are χ, the ratio of the magnitude of the velocity impulse to v_c (the circular speed in the disk), and the ratio $\gamma' = a/R_{max}$ describing the central concentration of the Plummer model.

We plot in Figure 2 the response of stars to the velocity impulse at a time equal to one-half a rotation period of the outer edge of the disk. The disk's rotation is counterclockwise. We randomly chose initial positions for 10^4 "stars" and plotted the positions according to our model at $\tau = 0.5$ [Radii, η, were chosen randomly in the interval $(0{:}\eta_{max})$, which produces a surface density that falls off as $1/\eta$ and is useful for illustrating particle kinematics.] In each column of Figure 2 the strength of the interaction, χ, and the softening parameter, γ', are held constant as the impact parameter is varied, taking values of 2.0, 1.0, 0.5, and 0.25 in units of the disk maximum radius (i.e., $\eta_{max} = 0.5, 1, 2, 4$). The impact distance from the center of the disk is indicated by the arrow at the bottom of each panel. The impact point is directly to the right of the disk center in the plots, and the scale is the same for all the panels of Figure 2. The central concentration, γ', has the value 0.4 in Figure 2*a*, 0.2 in Figure 2*b*, and 0.8 in Figure 2*c*. Representative values of $\chi = 0.25$, 0.50, and 0.75 were chosen for display. The most extreme combination of parameters strictly invalidates our assumptions in some regions of the disk but does not generally affect the overall morphology of the system.

The dependence of morphology on the three parameters is shown in Figure 2. More damage is done to the disks as the strength, χ, and the central concentration of the intruder (smaller γ') increase. The nonpenetrating collisions (the first two rows in Fig. 2, i.e., $\eta_{max} = 1, 0.5$) produce two-armed spiral features as exhibited in the n-body experiments of Toomre (1978). In the cases where the impact point is one-quarter the disk radius (row 4), rings form, although in the strongest interaction at this impact parameter ($\eta_{max} = 4$, $\chi = 0.75$, $\gamma' = 0.2$ in Fig. 2*b*) an arm also reaches outward through the disk. At intermediate impact parameters a one-armed spiral pattern is more prevalent. With decreasing impact parameters a tran-

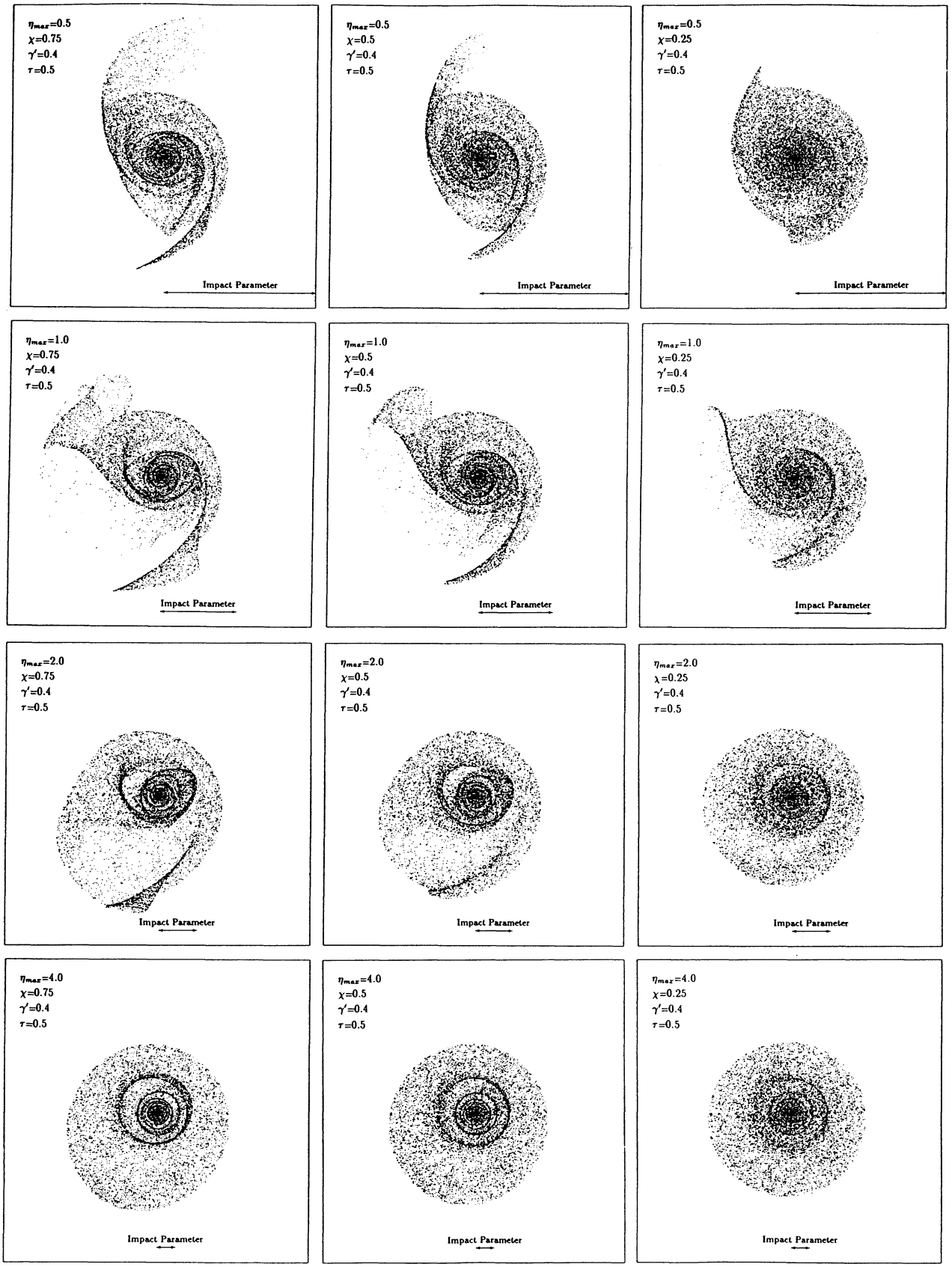

FIG. 2*a*

FIG. 2.—(*a*) Plots of disk particle positions as predicted by the analytic model. The time in each plot is one-half of a rotation period of the outer disk after impact. The impact parameter, as indicated by the arrow, varies down each column. The impact point is located on a line extending perpendicularly from the right-hand axis, passing through the disk center. The "strength" (see text) decreases in each row. The intruder central concentration parameter γ' is 0.4. (*b*) The same as (*a*), but with $\gamma' = 0.2$. (*c*) The same as (*a*), but with $\gamma' = 0.8$.

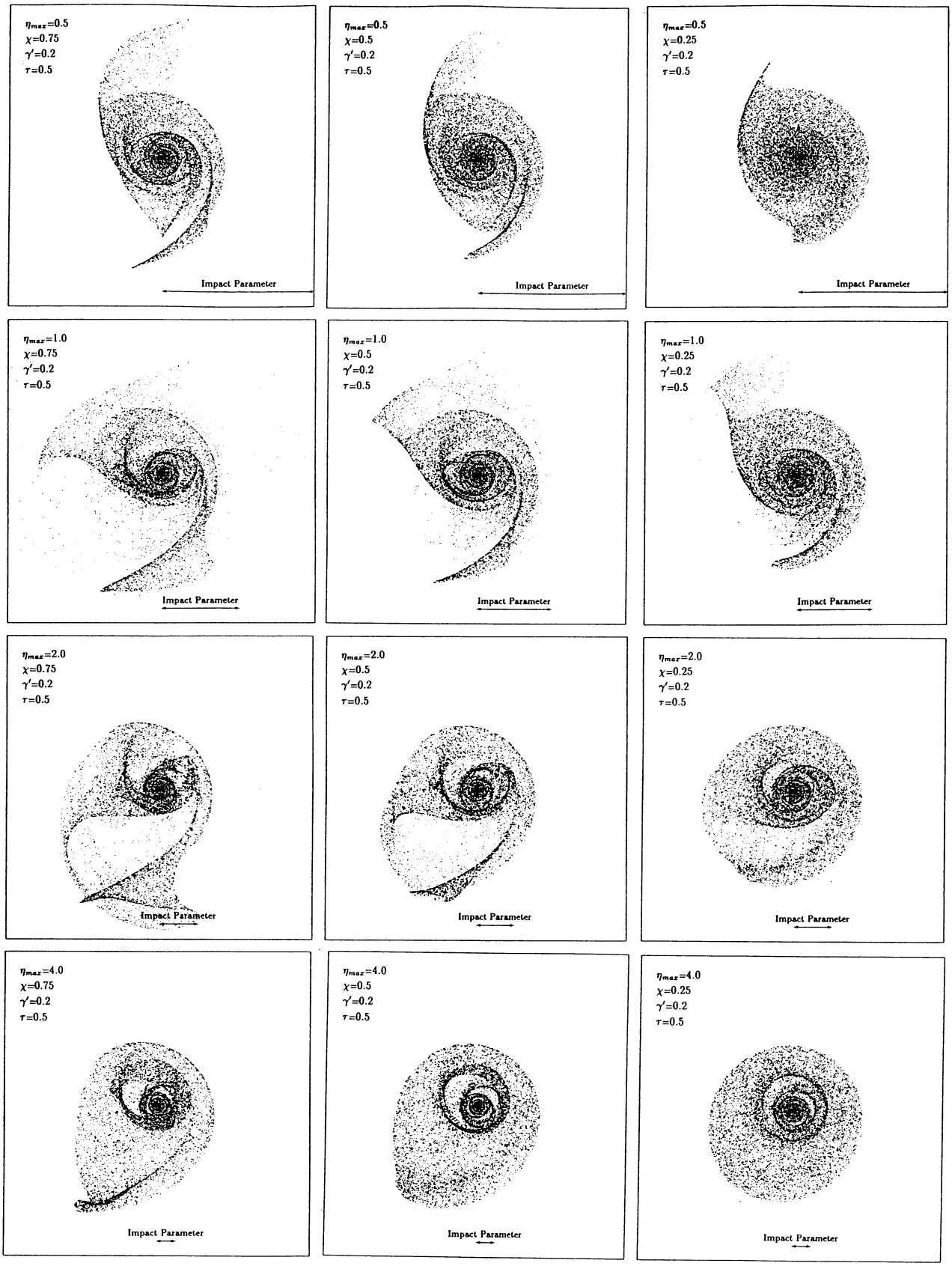

FIG. 2*b*

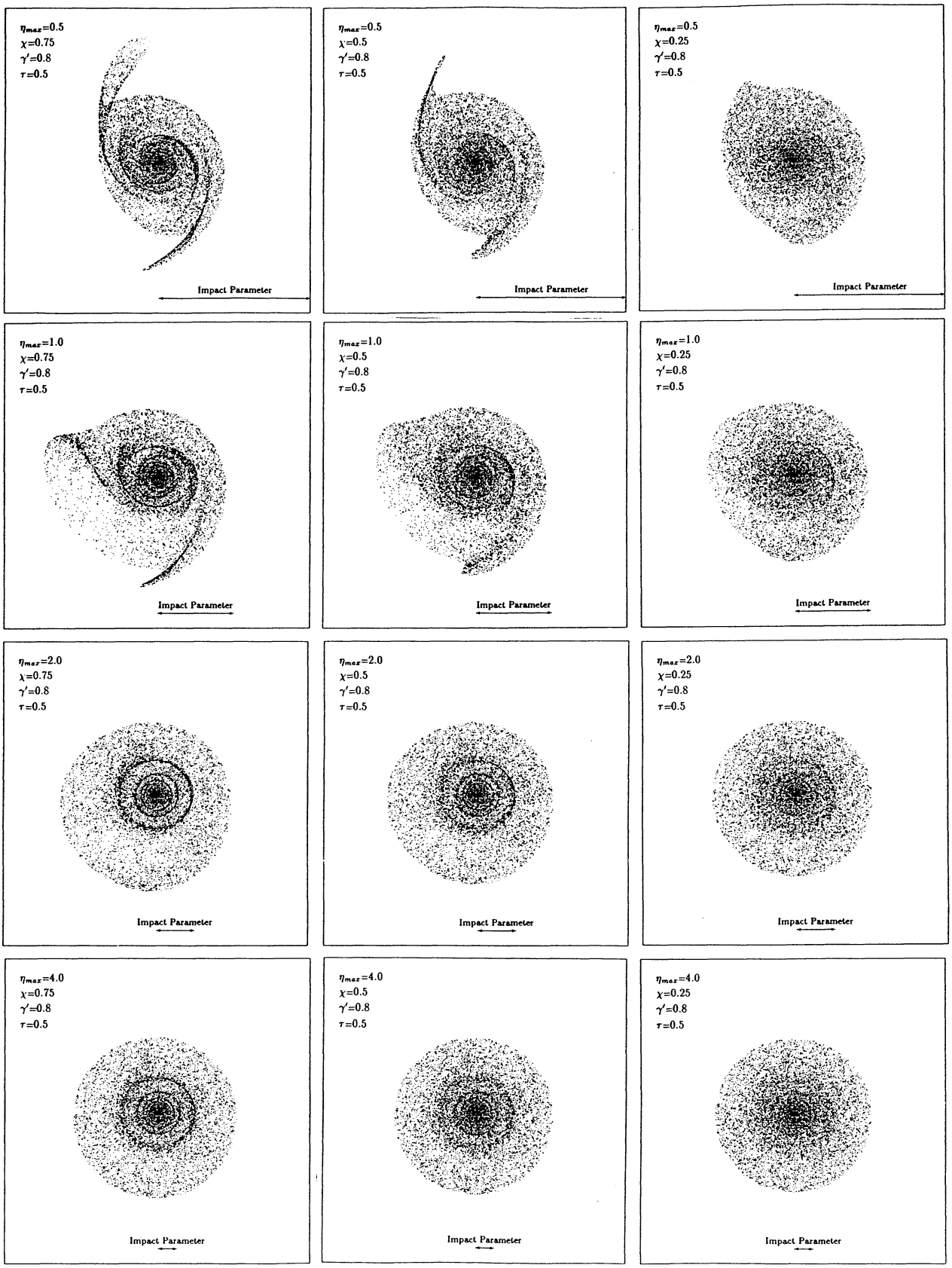

FIG. 2*c*

sition is seen that goes from two-armed spirals, through one-armed spirals, to formation of a ring. The transition from spiral to ring patterns appears to take place at impact parameters somewhere near 0.25 of a disk radius, approximately in agreement with the results of the n-body experiments of Lynds & Toomre (1976) and especially Toomre (1978). This agreement exists though Lynds & Toomre (1976) considered parabolic collisions with a 2:1 mass ratio between the galaxies, a situation in which one might not expect the impulse approximation to be applicable.

We can understand this transition qualitatively by considering the magnitude and directions of the imposed velocity impulses. In all cases there is a velocity component that produces a motion along the line connecting the disk center and the intruder. When the center of the intruder does not penetrate the disk, this takes the form of a tidal stretching along this line. Differential rotation shears this elongated form into a two-armed spiral pattern. When the intruder center penetrates the disk, however, on the impact side of the disk there is a compression, rather than a stretching, toward the impact point. The arm on that side of the disk disappears, being replaced by an arc that can appear as an inner ring, leaving the galaxy with one arm. As the impact point moves more toward the center, axisymmetry is approached and arms are replaced by rings.

As the strength parameter decreases, the galaxies become less distorted and the morphologies tend toward more symmetric forms. Likewise, as the intruder becomes more extended, nearly symmetric rings appear more often, as can be seen in the strong collision halfway out in the disk with an extended intruder ($\chi = 0.75$, $\gamma' = 0.8$ in Fig. 2c), which forms a ring.

In all cases a stronger collision with a more centrally condensed intruder produces sharper features. Off-center collisions produce orbit crossings, which lead to caustic formation, as pointed out by Struck-Marcell (1990) and Struck-Marcell & Lotan (1990). Most, if not all, of the caustic structures discussed in Struck-Marcell (1990) are evident here. The morphologies produced by our method in the grazing encounters ($\eta_{max} = 1$, 0.5) correspond closely to those found numerically by Byrd & Howard (1992) in a collision inclined by 40° to the disk normal. Their Figure 3 exhibits the same near- and far-side arm structure as seen in our model. Byrd & Howard (1992) suggest that encounters at approximately 60° from the disk normal are most common and are important for the formation of grand design spirals. The ring and arm morphology evident in Barnes' (1992) n-body study (see his Fig. 3) also mimics forms produced by our model.

3.2. *Lifetimes of Features*

Kinematic features typically appear to remain in the disk for tens of rotation periods of the outer disk before phase mixing washes out all obvious patterns (see § 1). With galactic disk rotation periods on the order of a few 10^8 yr, the kinematic features persist for 10^9 to 10^{10} yr. However, it might be expected that dynamical processes would completely dominate the disk evolution in a much shorter time. Sundelius et al. (1987) have shown in n-body experiments that tidal arms can last some 3×10^9 yr for a typical galaxy. Byrd & Howard (1992) conclude that these perturbations are important in driving spiral structure. Presumably, processes such as swing amplification (Toomre 1981) are contributing to the longevity of the spiral structure in the dynamical simulations as pointed out by Donner et al. (1991). Adams, Ruden, & Shu (1989) and Shu et al. (1990) have shown that one-armed spiral waves are formed in protostellar disks in which the center of mass does not coincide with the center of the potential.

4. EXAMPLE: FORMATION AND EVOLUTION OF SPIRAL FEATURES

As an example of how a self-gravitating disk behaves differently from the kinematic model, we examine one particular model in detail. We compare the behavior predicted by our analytic model response with that from a self-gravitating n-body/SPH simulation. We chose as our model one in which $2GM/Vbv_c = 0.2$, $\gamma' = 0.2$, and $\eta_{max} = 2.2$. If we scale parameters so that the disk galaxy resembles our own Galaxy, this model would correspond to physical parameters of $v_c = 220$ km s^{-1}, $b = 8$ kpc, $R_{max} = 17.6$ kpc, $M = 1.8 \times 10^{10}$ $M_\odot$ (intruder mass), $a = 3.5$ kpc, and $V = 580$ km s^{-1}. We note that these parameters are very similar to those used in Gerber et al. (1992), except the intruder mass is reduced by a factor of approximately 10. In that previous paper, Gerber et al. described the formation of a large-scale, incomplete ring of high stellar and gas density which resembled observations of the Arp 147 system. If we assume that the disk's constant circular speed is produced by a singular isothermal sphere density distribution, the mass interior to the edge of the disk is approximately 10 times the mass of the intruder. The rotation period of the outer edge of the disk is about 500 Myr. In all figures the disk rotation is again counterclockwise.

4.1. *Kinematic Response*

In the first panel of each row in Figure 3 we show a time sequence of the disk response to the above perturbation as given by our analytic model. By $\tau = 0.10$, a prominent arc of enhanced density has formed. A careful inspection of particle orbits in the vicinity of the arm reveals that particles that initially lay on a common circle have crossed the orbits of particles that were originally farther out in radius. This crossing occurs in part because the epicycle frequency in the disk is larger at smaller radii, so that stars near the center of the potential begin moving outward while stars further out are still falling in. This will have consequences when we consider gas interactions in this region (see § 2.4). If these particles represented gas, they would not be able to stream freely past one another and would interact strongly.

The arm continues to unwind in subsequent rows in Figure 3, and a low density region forms interior to the arc. At $\tau = 0.30$, there appear to be two arms on one side of the disk, bracketing a region with very few stars. The prominent features at $\tau = 0.51$ are a diffuse single arm which loops toward the bottom of the figure and an inner arm with adjacent low-density region in the upper left-hand quadrant.

We can gain insight into the process which forms the first prominent arm by examining a small number of rings of particles as shown in Figure 4. Notice in particular the second ring out at $\tau = 0.05$. The kink forms due to the differential angular momentum impulse delivered to particles on opposite sides of the horizontal axis. Particles on the side of the impact in the direction of rotation (upper-right quadrant in the panels of Fig. 4) lose angular momentum as a result of the impulse. In this approximation, they instantaneously find themselves moving too slowly to maintain a circular orbit and begin to fall inward. Particles on the other side of the impact point receive an angular momentum boost. They respond by moving outward

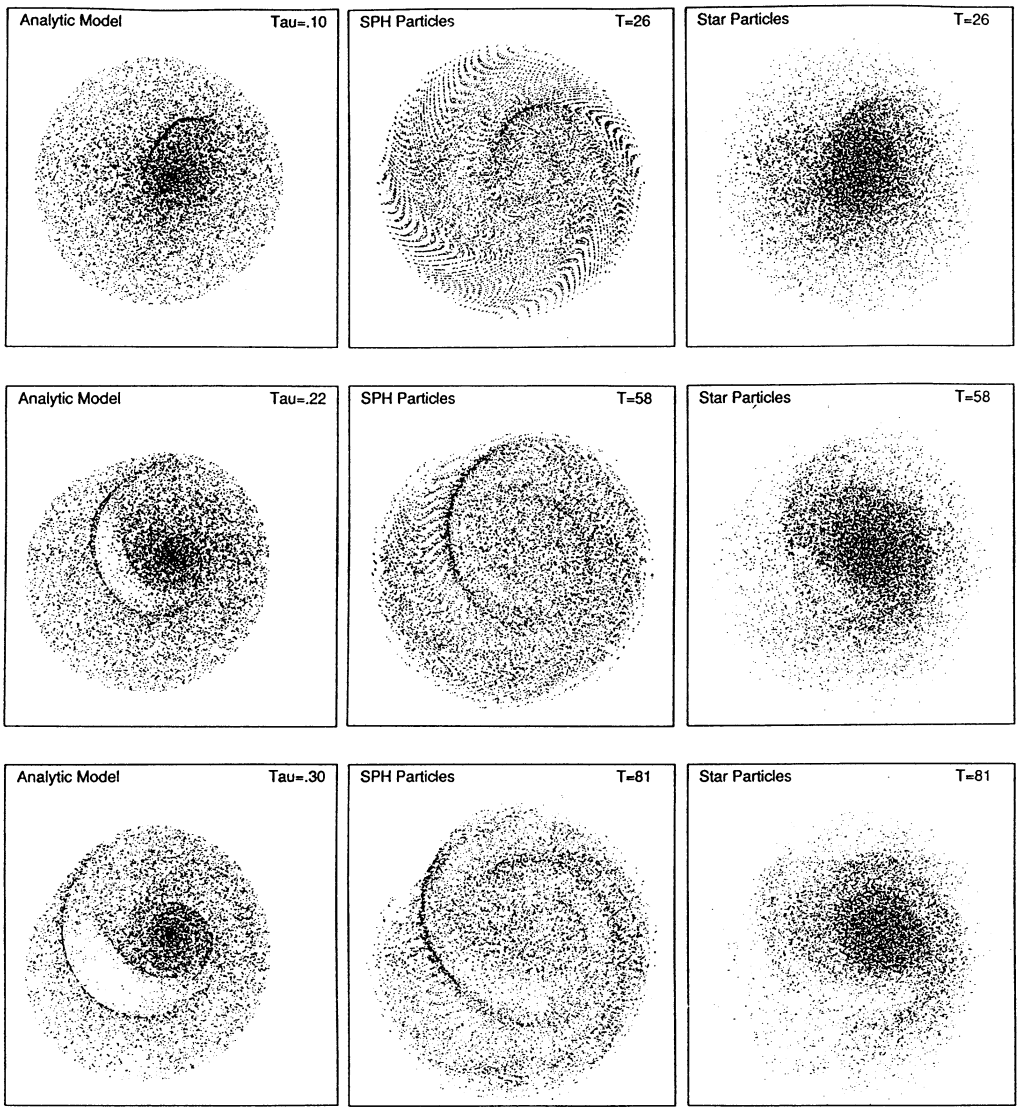

FIG. 3.—Plots of particle positions for the example collision described in § 4. The first plot in each row represents the analytic model, the second plot shows the SPH particles from the dynamic calculation, and the third plot shows the corresponding n-body disk particle positions.

in radius. All the particles at the same radius get an azimuthal velocity impulse directed toward the impact point, so that there is also a compression along the ring and the density increases near the kink. The arm begins to grow at the locus of these kinks, and by $\tau = 0.10$ orbits are crowding together and can be seen to cross one another at $\tau = 0.15$.

4.2. *Dynamic Response*

To study the dynamic response of the disk to the collision, we employed a three-dimensional n-body stellar dynamic and SPH program developed by D. S. Balsara (see Balsara 1990; Gerber 1993). All components—the disk stars and gas, the disk galaxy halo, and the intruder stars—contribute to the gravitational potential and are free to respond to the time-dependent forces generated by that potential. The computations were performed on the Cray 2 supercomputer at the National Center for Supercomputing Applications at the University of Illinois at Urbana-Champaign.

4.2.1. *Numerical Method*

In SPH, particles are used to model the gas continuum. The particles carry with them information about their position, thermal energy, and velocity. The density is obtained by smoothing out the mass of neighboring particles using an analytic smoothing function (see Lucy 1977; Gingold & Monaghan 1977; Hernquist & Katz 1989; Balsara 1990). In the simulations reported here, we use an ideal gas equation of state and enforce isothermality by having each SPH particle retain its initial temperature (see Gerber 1993; Gerber et al. 1992, 1994a).

The gravitational force is calculated by standard PM techniques (see Hockney & Eastwood 1988). The gravitational potential is calculated only at a restricted number of points on a three-dimensional grid, and fast Fourier transform techniques are used to solve Poisson's equation on the grid and thus determine the gravitational potential. Forces are found by differencing the potential, and the force on an individual particle is determined by interpolation between grid points. In the

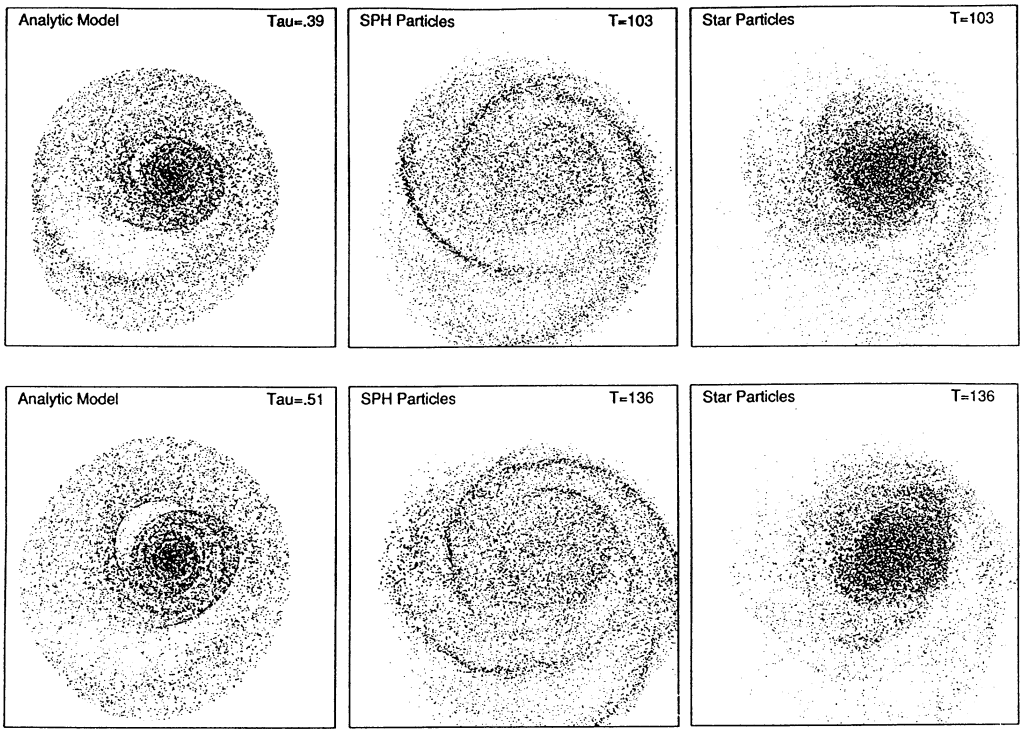

FIG. 3—*Continued*

experiments described in this paper we use a cubic grid with 64 points along each side. Time integration is performed using a time-centered leapfrog method (see Hockney & Eastwood 1988). More details of the combined code can be found in Gerber et al. (1994a) and Balsara (1990), where tests of it are presented.

4.2.2. *Model Galaxies*

The model disk galaxy consists of an exponential disk of gas and stars surrounded by a massive, almost spherical halo of gravitationally active particles. The elliptical galaxy consists of a spherical distribution of stars only. The stellar disk with surrounding halo was constructed in a manner similar to that described in Barnes (1988). That is, the halo was allowed to relax as an exponential disk potential was slowly imposed over several halo crossing times. The halo was originally a spherical King model (King 1966; Binney & Tremaine 1987) consisting of 25,000 particles. The disk has a mass $\frac{2}{5}$ that of the halo and has 25,000 particles in rotation around the center. Toomre's stability parameter, Q, (Toomre 1964) was set fo 1.5 everywhere in the disk. The three-dimensional density distribution, ρ, of the disk is

$$\rho(R, z) = \frac{\Sigma(R)}{2H} \operatorname{sech}^2 \frac{z}{H}, \tag{27}$$

where $H = \sigma_z^2(R)/\pi G\Sigma(R)$, and $\Sigma(R) = (M_{\rm exp}/2\pi R_d^2) \exp(-R/R_d)$. Here $\sigma_z^2(R)$ is the velocity dispersion in the z direction. The scale height, H, was set to a constant value throughout the disk; $M_{\rm exp}$ is the total mass of a radially infinite exponential disk with disk radial scale length, R_d. The disk density distribution was cut off at $4.4\,R_d$.

Approximately 22,000 SPH particles were distributed throughout the disk to represent a gaseous medium of mass 1/10 that of the stellar disk. The SPH particles were placed in circular orbits around the center of the disk with a small correction made to the circular speed to account for radial pressure gradient support. The gas-free elliptical galaxy was represented by a spherical King model. More details of the initial models can be found in Gerber (1993) and Gerber et al. (1992, 1994a).

The parameters of the computational model galaxies correspond closely to those of the analytic model of § 4.1, but there are some differences. The computer model's disk rotation curve rises from the center, reaches a peak value at a radius of about $2R_d$, and then slowly falls out to the edge of the disk, unlike the constant circular velocity model assumed in the analytic treatment. The chosen King model's mass and radius yield a potential that approximates the potential form of the Plummer model given previously. The dimensionless combination of simulation constants $2G\alpha M_{\rm King}/bV_{\rm max}v_{c,\rm avg}$ has the approximate value 0.2. Here $M_{\rm King}$ is the King model mass, α is a constant of order unity (1.24 in this case) that is used to scale the King model potential to that of the corresponding Plummer model, b is the distance of closest approach of the two galaxies' centers of mass, $V_{\rm max}$ is the maximum relative velocity of the centers of mass, and $v_{c,\rm avg}$ is the value of the circular rotation speed averaged over the disk stars.

With the scaling given at the beginning of this section, the disk galaxy has a mass of $1.75 \times 10^{11}\ M_\odot$, one exponential disk scale length equals 4 kpc, and one time unit is 2 Myr. The intruder galaxy has a mass of $1.75 \times 10^{10}\ M_\odot$. The disk has a total mass of $5 \times 10^{10}\ M_\odot$ (10% of which is gas) and the halo mass is $1.25 \times 10^{11}\ M_\odot$. The vertical scale height in the disk is 800 pc, somewhat larger than that seen in real spiral galaxy disks but used here to avoid large gradients on length scales beneath our numerical resolution. A disk 800 pc thick is still quite thin compared to its diameter, which is truncated at

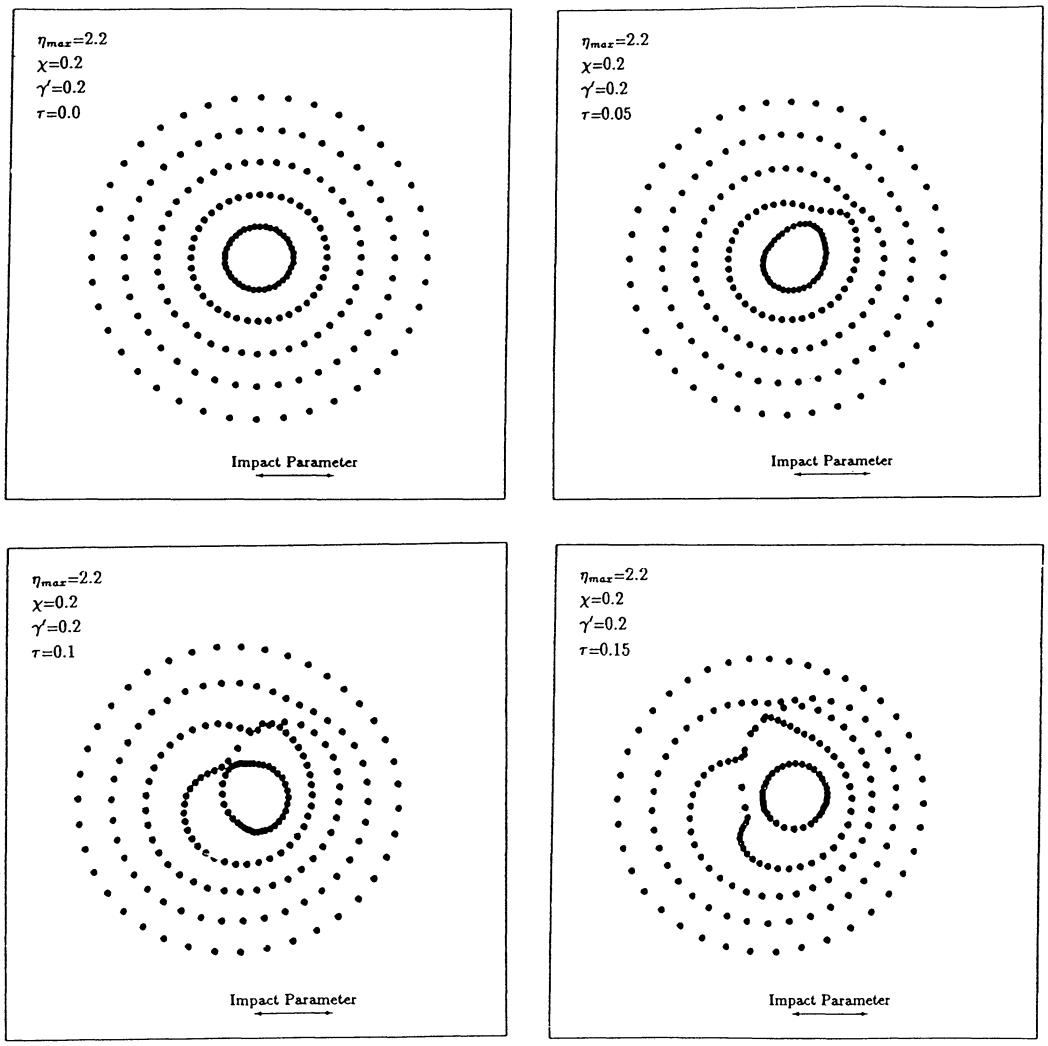

FIG. 4.—The same analytic model as shown in Fig. 3, but with a smaller number of particles plotted. The time sequence highlights how the differential angular momentum impulse distorts initially circular rings and leads to the formation of the initial arm seen in Fig. 3.

35 kpc. The disk rotation velocity, averaged over the entire disk for this model, is 211 km s^{-1}. The gas density in the plane of the disk ranges from about 0.025 amu cm^{-3} at the outer edge to about 2 amu cm^{-3} at the center of the disk. The ratio of temperature to mean molecular weight, T/μ, varies from 8000 K at the outer edge of the disk to 6×10^5 K at the center. This temperature is required to provide enough gas pressure to support the disk against gravity in the perpendicular direction. Support due to magnetic fields and cosmic rays is not considered here. The model for the gas is not meant to accurately model any one single component of the interstellar medium; rather, it is to be thought of as representing a collisional component in the disk that captures some of the physics relevant to star formation studies, such as increases in density and the presence of shocks.

4.2.3. *Results and Comparison to Analytic Model*

The distribution of gas and stellar particles are shown projected onto the x-y plane in the second and third panels, respectively, of Figure 3. Only disk particles are shown, and rotation is counterclockwise. Time is reckoned from the time of close approach of the two galaxies' centers of mass. The τ given in the analytic expression corresponds to 265 units of simulation time, T, or 530 Myr.

Caution should be used when interpreting the SPH plots in Figure 3. Each particle has (in principle) a different mass, so regions of high particle density do not necessarily indicate a correspondingly high gas density. Rather, it is better to loosely think of regions of high SPH particle density as indicating a high density *relative to the initial density in the unperturbed disk*. On the other hand, the stars all have the same mass, and an apparent high density does indicate a correspondingly high stellar surface density.

Despite the differences between the analytic form for the disk potential and that of the computer model, the behavior of the disk in the latter is similar to that seen in the former. At $T = 26$ the arm-like feature seen at $\tau = 0.10$ shows up clearly in the SPH particles and is visible as a broader density enhancement in the stars. That arm continues to develop as it did in the analytic model, and by $T = 81$ ($\tau = 0.30$) a counterarm has formed that does not have an obvious analog in the analytic model. Self-gravity and dissipation in the disk galaxy are likely important in the formation of this feature. Either a small density enhancement is being locally amplified in the disk, or

the disk is responding to its own global nonaxisymmetric potential, the symmetry having been disrupted by the passage of the intruder. Probably both processes are at work here.

Kinematic features are still quite evident at $T = 103$ ($\tau = 0.39$). The arm in the lower left-hand quadrant continues to be strongly visible in the SPH particles, even though stars are no longer present in either the analytic or computer models. The small spur interior to this arm that appears in the analytic model is evident, particularly in the plot of stars. The kinematic model gives reasonable results even as late as $T = 136$ ($\tau = 0.51$). The inner arm that ends in the lower right-hand quadrant and winds into the nucleus (see the plot of stars) is predicted by the analytic model, as is the low stellar density region just outside that arm at the lower right. The gap just to the upper left of the nucleus likewise shows up in the kinematic model, as does the general oval shape of the inner part of the galaxy. A mismatch between the form and magnitude of the analytic and computer models' rotation curves becomes apparent by the end of our computational run at $T = 158$ ($\tau = 0.59$); the computer galaxy, which has a peak circular speed greater than the analytic model's circular speed, is running ahead of the kinematic model, but the general features are still present.

The ultimate dynamic fate of the disk is uncertain. The disturbances set up in the disk could initiate the self-amplification and feedback loop as discussed by Toomre (1981) to produce long-lived spiral features (see Byrd & Howard 1992). Even in the absence of this mechanism, the kinematic response has a memory of many tens of disk rotation periods as discussed previously, which could provide the seeds for further growth of disk instabilities.

4.2.4. *Response of Gas versus Stars*

The collisionless stars and dissipational gas respond differently following the interaction and may have differing spatial distributions at any given time. The SPH particles, which were initially on circular orbits, as were the stars in the analytic treatment, exhibit thin features which resemble the analytic model at early times after passage of the intruder. The stars show these same features, but they are much broader, owing to their initial velocity dispersion. When orbits which were initially circular cross, the gas is compressed, serving to further enhance the kinematic features in the plots of the SPH particles but also decoupling the gas from the stellar flow. Neighboring gas particles become correlated in phase (position and velocity) space after a momentum conserving inelastic collision, and, because of this, features can remain in the gas after the corresponding stellar patterns have disappeared. For this reason the plots of disk stars more resemble our analytic model at later times after the collision.

If we assume that elevated star formation rates correlate in some manner with high SPH gas density and shock locations (see, e.g., Mouschovias, Shu, & Woodward 1974), our computer simulation shows that enhanced levels of star formation can occur at sites where there is no underlying old stellar population. This occurs when stellar kinematic features disappear due to the stars' ability to freely stream past one another, but inelastic collisions force gas, from which stars form, to be left behind. An observational consequence of this scenario is that we would expect to find some features in interacting systems that contain many young stars with no significant corresponding background old stellar feature.

In an upcoming paper (Gerber et al. 1994b) we show numerically that off-center collisions, similar to those considered here, produce larger gas density enhancements and strong shocks in the outer regions of the disk when compared to central collisions. The mechanism that produces the high gas densities is the interplay between the intersecting orbits discussed here. When the collision is off center, the large rotational kinetic energy of the disk is tapped to produce strong dissipation in the gas. In collisions between equal-mass galaxies, orbits are perturbed strongly and gas interacts violently, and a significant decoupling between stars and gas occurs.

5. SUMMARY

We have derived a kinematic model for the collision of a disk galaxy with a small, fast spherical galaxy whose impact trajectory is parallel to the disk galaxy's rotation axis and passes through the disk at an arbitrary distance from its center. This model shows that the morphological forms found in the n-body experiments of Toomre (1978) and Byrd & Howard (1992) can be understood in terms of stars executing epicyclic oscillations about a circular guiding center in the plane of the disk after receiving a velocity impulse from a second galaxy. The resulting morphologies depend on the "strength" parameter (which includes the mass and relative velocity of the intruder), the impact parameter, and the central concentration of the intruder. Distant encounters produce transient two-armed spiral features, collisions through the outer parts of the disk make one-armed spirals, and central collisions produce rings.

Comparison with a fully self-gravitating n-body/gasdynamics computer simulation shows that the disk response is largely kinematic at early times after passage of the intruder. Gas, which was initially in circular orbits, shows a strong density enhancement in the region where those circular orbits cross. The stellar distribution is much broader owing to its initial velocity dispersion and collisionless nature. At later times (a significant fraction of a rotation period of the outer edge of the disk), the self-gravity of the disk, which was somewhat prone to developing nonaxisymmetric structure in the first place (see Gerber 1993; Gerber et al. 1994a), can become important in amplifying density perturbations.

We expect that star formation is triggered in regions of strong gas interactions, such as the regions of orbit crossings. Gas streams collide inelastically in these regions, which produces large density enhancements and decouples gas from the flow of stars. This separation of stellar and gaseous density enhancements leads us to predict that active star formation can occur in regions where there is currently no significant underlying old stellar population.

We would like to thank D. S. Balsara for use of his implementation of the n-body/SPH code. C. Struck-Marcell provided many helpful comments and suggestions. We gratefully acknowledge the support of NASA graduate student training grant NGT 70041, NASA grant NAG 5-1241, University of Illinois Research Board grants, the National Research Council, and NASA/Ames Research Center. All numerical calculations were performed at the National Center for Supercomputing Applications at the University of Illinois, under funding from the National Science Foundation.

REFERENCES

Adams, F. C., Ruden, S. P., & Shu, F. H. 1989, ApJ, 347, 959
Appleton, P. N., & Struck-Marcell, C. 1987a, ApJ, 312, 566
———. 1987b, ApJ, 318, 103
Balsara, D. S. 1990, Ph.D. thesis, Univ. of Illinois at Urbana-Champaign
Barnes, J. E. 1988, ApJ, 331, 699
———. 1992, ApJ, 393, 484
Binney, J., & Tremaine, S. 1987, Galactic Dynamics (Princeton: Princeton Univ. Press)
Byrd, G. G., & Howard, S. 1992, AJ, 103, 1089
Chatterjee, T. K. 1984, Ap&SS, 106, 309
———. 1986, Ap&SS, 121, 213
Donner, K. J., Engström, S., & Sundelius, B. 1991, A&A, 252, 571
Fosbury, R. A. E., & Hawarden, T. G. 1977, MNRAS, 178, 473
Gerber, R. A. 1993, Ph.D. thesis, Univ. of Illinois at Urbana-Champaign
Gerber, R. A., Lamb, S. A., & Balsara, D. S. 1992, ApJ, 399, L51
———. 1994a, MNRAS, submitted
———. 1994b, in preparation
Gingold, R. A., & Monaghan, J. J. 1977, MNRAS, 181, 375
Hernquist, L., & Katz, N. 1989, ApJS, 70, 419
Hernquist, L., & Weil, M. L. 1993, MNRAS, 261, 804
Higdon, J. L. 1993, Ph.D. thesis, Univ. of Texas
Hockney, R. W., & Eastwood, J. W. 1988, Computer Simulations Using Particles (Bristol: Adam Hilger)
Huang, S., & Stewart, P. 1988, A&A, 197, 14
King, I. E. 1966, AJ, 71, 64
Lynds, R., & Toomre, A. 1976, ApJ, 209, 382
Lucy, L. B. 1977, AJ, 82, 1013
Marcum, P., Appleton, P., & Higdon, J. 1992, ApJ, 399, 57
Mouschovias, T. Ch., Shu, F. H., & Woodward, P. R. 1974, A&A, 33, 73
Plummer, H. C. 1911, MNRAS, 71, 460
Schultz, A. B., Spight, L. D., Colegrove, P. T., & DiSanti, M. A. 1990, Poster paper presented at the STScI workshop "Massive Stars in Starbursts"
Schultz, A. B., Spight, L. D., Rodrigue, M., Colegrove, P. T., & DiSanti, M. A. 1991, BAAS, 23, 953
Shu, F. H., Tremaine, S., Adams, F. H., & Ruden, S. P. 1990, ApJ, 358, 495
Struck-Marcell, C. 1990, AJ, 99, 71
Struck-Marcell, C., & Appleton, P. N. 1987, ApJ, 323, 480
Struck-Marcell, C., & Higdon, J. L. 1993, ApJ, 411, 108
Struck-Marcell, C., & Lotan, P. 1990, ApJ, 358, 99
Sundelius, B., Thomasson, M., Valtonen, M., & Byrd, G. G. 1987, A&A, 174, 67
Theys, J. C., & Spiegel, E. A. 1976, ApJ, 208, 650
———. 1977, ApJ, 212, 616
Thompson, L. A., & Theys, J. C. 1978, ApJ, 224, 796
Toomre, A. 1964, ApJ, 139, 1217
Toomre, A. 1978, in IAU Symp. 79, Large-Scale Structure of the Universe, ed. M. S. Longair & J. Einasto (Dordrecht: Reidel), 109
Toomre, A. 1981, in The Structure and Evolution of Normal Galaxies, ed. S. M. Fall & D. Lynden-Bell (Cambridge: Cambridge Univ. Press), 111
Toomre, A., & Toomre, J. 1972, ApJ, 178, 623